Microfluidics and Nanofluidics (2026) 30:16
https://doi.org/10.1007/s10404-025-02869-6

CORRESPONDENCE

# Numerical simulation and validation of stretchable inertial microfluidics for tunable particle focusing and separation

**Shaghayegh Tavasoli[1] · M. Soltani[1,2,3,4] · Mohammad Kiani Shahvandi[1] · Navid Kashaninejad[5] · Nam-Trung Nguyen[5]**

Received: 30 July 2025 / Accepted: 23 December 2025


**Abstract**
Inertial microfluidics is a passive particle manipulation technique, excelling in simplicity, precision, and high throughput. However, its restricted adaptability to varying particle sizes has limited its broader application. This study presents numerical simulations on a stretchable inertial microfluidic device that dynamically adjusts channel dimensions, enabling tunable particle focusing and separation. Building upon the experimental work by Fallahi et al. (Analytical Chemistry, 2020), we incorporate advanced numerical simulations to evaluate how channel stretching influences particle migration dynamics. We investigate the inertial focusing of 15 µm particles and the separation of 10-µm and 15-µm particles in a straight channel under varying stretching lengths. Stretching the channel length up to 6 mm resulted in a near-complete focusing efficiency of almost 100%. Furthermore, increasing the channel length enhanced the effective separation of 10- and 15-µm particles, achieving 100% separation efficiency and purity. We identify an optimal stretching length that maximizes the separation efficiency, thereby confirming the device's effectiveness. Qualitative and quantitative validation demonstrate excellent agreement between experimental and simulation results, with an accuracy of 99.82% and an average error of 0.18%, underscoring the reliability of the proposed model. The simulated stretchable device, capable of dynamically adjusting the channel dimensions in real time, opens up new perspectives and potential applications with enhanced tunability and performance of inertial manipulation, focusing, and separation of particles.

**Keywords** Inertial microfluidics · Stretchable microfluidics · Flexible microfluidic devices · Particle focusing · Particle separation · Numerical simulation

## 1 Introduction

Recently, significant attention has been given to developing techniques for manipulating bioparticles and cells (Hettiarachchi et al. 2023) in biomedical (Li et al. 2018), biological (Mukherjee et al. 2024; Scheler et al. 2019; Tajik et al. 2019), and chemical (Zhang et al. 2020) applications. These applications require precise manipulation of biological samples, such as focusing, separation, and isolation, which are crucial for advancing fields such as basic research (Yang et al. 2020; Sajeesh and Sen 2014), clinical applications (Gharib et al. 2022; Contreras-Naranjo et al. 2017), and drug discovery (Kimura et al. 2018). Various techniques have been proposed for cell focusing and separation. While these methods enable optimal focusing and separation, they often suffer from drawbacks such as being time-consuming, overly complex, and high-cost (Hettiarachchi et al. 2023). In contrast, microfluidic systems meet the needs for the handling and manipulation of liquid samples, suspended cells,

✉ M. Soltani
msoltani@uwaterloo.ca

[1] Department of Mechanical Engineering, K. N. Toosi University of Technology, Tehran, Iran

[2] Department of Electrical and Computer Engineering, University of Waterloo, Waterloo, Canada

[3] Centre for Biotechnology and Bioengineering (CBB), University of Waterloo, Waterloo, Canada

[4] Department of Integrative Oncology, BC Cancer Research Institute, Vancouver, Canada

[5] Queensland Micro- and Nanotechnology Centre, Nathan Campus, Griffith University, 170 Kessels Road, Brisbane QLD 4111, Australia

Published online: 19 January 2026

and biological particles, toward personalized medicine and innovative therapies (Chrimes et al. 2013; Ayuso et al. 2022; Park et al. 2024).

Microfluidic approaches are broadly categorized based on the sources of manipulation forces as passive and active techniques (Cha et al. 2022). Active techniques (Grier 2003, Çetin and Li 2011; Wang and Zhe 2011; Zhou et al. 2023) utilize external force fields, such as magnetophoresis (Giudice et al. 2015; Forbes and Forry 2012), dielectrophoresis (Zhou et al. 2018, 2020a, 2020b), electrophoresis (Jeon et al. 2016), and acoustophoresis (Zhang et al. 2018a, 2018b), whereas passive techniques (Yamada and Seki 2005; Huang et al. 2004; Altmann and Ripperger 1997; Yamada et al. 2004; Carlo 2009; Zhou and Papautsky 2013; Zhang et al. 2016) rely on channel geometry and hydrodynamic forces (Zhang et al. 2014). Among passive methods, inertial microfluidics exclusively uses hydrodynamic forces for focusing and separating cells and other bioparticles (Bogseth et al. 2020). This approach offers remarkable characteristics, including ease of operation, precise manipulation capabilities, high throughput, and cost-effective implementation (Zhang et al. 2016). For example, Zhou et al. (2013a, 2013b) demonstrated that hydrodynamic particle focusing can be effectively used for passive, sheathless particle focusing in microfluidic channels. Inertial migration refers to the phenomenon where cells or particles randomly distributed at the entry of a straight channel gradually migrate transversely to equilibrium positions in the cross-section after traveling a sufficient distance (Segre and Silberberg 1961, 1962). This process relies on two dominant forces: the shear gradient lift force ( $F_S$), which moves particles from the channel center towards its wall, and the wall-induced lift force ( $F_W$), which propels particles away from the wall towards the center. The balance between above-mentioned forces leads to the formation of equilibrium positions in the channel cross-sections. (Zhang et al. 2016; Segre and Silberberg 1961). The performance of inertial microfluidic systems is influenced by critical parameters such as channel geometry, flow rates, flow rate ratios (FRRs), and the resistances of outlet channels (Bogseth et al. 2020; Tu et al. 2017; Wang and Papautsky 2015; Zhou et al. 2013a, 2013b; Chung et al. 2013).

Advances in microfluidics enable highly efficient platforms for focusing and separating particles and cells. Hence, extensive research has been carried out to enhance the efficiency of particle focusing and separation using inertial microfluidics. Zhou et al. (2013a, 2013b) developed a microfluidic system that utilizes two-stage inertial migration to effectively separate particles and rare cells in the blood. The system employs a straight rectangular microchannel with variable aspect ratios to enable precise control of the flow field and particle trajectories (Zhou et al. 2013a, 2013b). Tu et al. (2017) introduced a parallel inertial microfluidic system for size-based particle focusing, offering an adjustable cutoff size through output resistance manipulation. Bogseth et al. (2020) developed a co-flow inertial microfluidic device to focus particles according to their size, analyzing the effects of flow rate, FRRs, and channel resistance ratio on tunability and separation performance. Zhang et al. (2023) investigated size-based particle separation using sheath flows, demonstrating the influence of flow rate and channel length. Zhang et al. (2018a, 2018b) introduced a microfluidic system that combines dielectrophoresis with inertial flow to demonstrate tunable particle separation. Zhou et al. (2019) utilized a microfluidic platform with a straight inertial migration channel and multi-flow to separate circulating tumor cells (CTCs) according to their size. In addition, Zhou et al. (2020a, 2020b) employed non-Newtonian viscoelastic fluids to focus and separate elasto-inertial particles, enabling tunable particle separation. Mashhadian and Shamloo (2019) analytically studied particle focusing in inertial microfluidics within rectangular microchannels and demonstrated that equilibrium positions are governed by particle size, channel aspect ratio, and Reynolds number. Raufi et al. (2019) experimentally and numerically explored particle focusing in straight microchannels using viscoelastic fluids, highlighting how cross-sectional geometry and flow rate influence the focusing behavior in elasto-inertial microfluidic systems. Nouri et al. (2024) numerically investigated the elasto-inertial particle focusing in straight and serpentine microchannels using DNS in a viscoelastic medium.

Despite extensive studies to achieve tunable focusing and separation performance, most devices introduced so far have fixed configurations that cannot be altered or adjusted after fabrication, limiting their use to a specific particle size. In reality, samples vary in size, necessitating devices with adjustable designs for precise manipulation. Enhancing the device's efficiency for focusing and separating particles of different sizes requires iterative channel design, extensive testing on samples, and optimization of operating conditions (Bogseth et al. 2020). These steps, however, are cumbersome, time-consuming, and costly, emphasizing the need for further research to develop optimal configurations that improve the efficiency of particle focusing and separation techniques.

Recently, flexible and stretchable microfluidic platforms have emerged, offering a suitable solution for the development of devices and systems with special requirements. This advancement enabled new applications in medicine, biology, chemistry, and electronics (Fallahi et al. 2019, 2021; Pinho et al. 2019; Baek et al. 2005; Vu et al. 2023). While

this research area is rapidly evolving and has gained significant traction in biomedical technologies and diagnostic applications, it requires further comprehensive exploration. Fallahi et al. (2020) introduced and demonstrated experimentally a flexible inertial microfluidic device capable of precise tuning of channel dimensions. The team assessed the focusing and separation behavior of a mixture of two particles in a straight microchannel under various stretching lengths. Subsequently, they demonstrated the capability to tune and control the separation threshold for a particle mixture using a stretchable inertial microfluidic device. Furthermore, the team demonstrated focusing and separation of CTCs from diluted whole blood and white blood cells (Fallahi et al. 2021). These systems provide greater tunability and control over particle manipulation, addressing the limitations of devices with fixed geometry.

Computer simulations are essential tools for designing and optimizing microfluidic devices. These tools allow for exploring design spaces, optimizing geometries, and analyzing functional parameters that are experimentally costly, time-consuming, and challenging (Shahvandi et al. 2023; Kiani Shahvandi et al. 2022; Souri et al. 2023). By streamlining research processes, simulations support experimental work through system behavior analysis and performance prediction, significantly reducing reliance on trial and error while minimizing time and costs (Sheidaei et al. 2020; Erickson 2005; Carvalho et al. 2021).

This study proposes and develops a mathematical framework. To validate the proposed approach, numerical simulations replicating a real experiment on a stretchable microfluidic system were carried out, demonstrating high-precision particle focusing and separation via inertial focusing. Unlike prior studies, our work systematically determines optimal stretching conditions for enhanced performance, bridging the gap between fixed-geometry devices and adaptive microfluidic platforms. Such simulation provides an opportunity to optimize stretching lengths, flow conditions, and particle sizes prior to experimental testing and fabrication. The migration trajectories of 15 µm particles were analyzed under different stretching lengths to assess focusing efficiency. Additionally, a binary particle mixture (10 µm and 15 µm) was examined under different stretching lengths to evaluate separation capabilities. These simulations, while validating the experimental findings reported by Fallahi et al. (2020), effectively addressed existing gaps by providing detailed analyses of particle behavior and separation mechanisms in stretchable inertial microfluidic systems. The simulation analyses demonstrate that stretchable microfluidic devices not only allow post-fabrication channel adjustment but also significantly enhance the precision of particle focusing and separation. Additionally, the simulation of stretchable inertial microfluidics allows for determining the optimal stretch length, facilitating the effective separation of particles and cells with varying sizes. This approach improves efficiency while offering substantial savings in processing time and costs associated with design, testing, fabrication, and re-optimization.

## 2 Materials and methods

This section provides a detailed description of the computational geometry of the channel, the difference in particle lateral displacement ratio, and the effects of channel stretching on the lateral migration of particles. It also covers hydrodynamic forces acting on the particles, governing equations for fluid flow analysis, and particle trajectories. Finally, the solution strategy section details initial and boundary conditions, physics, solver settings, and other simulation parameters. The equations and parameters of this mathematical framework were derived through an in-depth review of experimental, numerical, and analytical studies in the field of microfluidics, particularly in the areas of particle tracing and fluid flow. By intelligently integrating these equations into a unified framework, we numerically reproduced, with high accuracy, the physical behavior of an experimental microfluidic system developed by Fallahi et al. (2020), based on the conditions reported in their study.

### 2.1 Computational geometry

The computational model is based on the previously reported stretchable inertial microfluidic device (Fallahi et al. 2020). Figure 1 depicts the three-dimensional (3D) numerical model. The geometry includes two inlets (central sheath flow and bifurcating particle inlets), a central

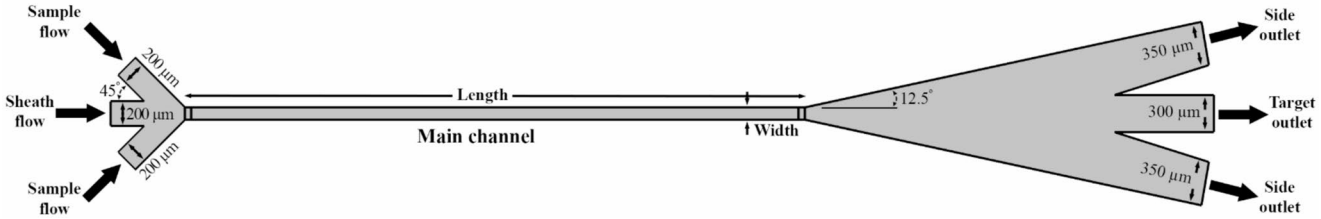


**Fig. 1** Schematic illustration of the stretchable inertial microfluidic device, showing the main straight channel with central and side inlets for sample and sheath flows, and three outlet channels (target and side outlets) used for size-based particle separation

microchannel, and two outlets. Stretching the channel alters its length and width while maintaining a constant aspect ratio $(H/W \approx 0.5)$. The strain ratio $(\epsilon)$ for particle focusing and separation is defined as the ratio of the stretching length $(\Delta L_{f.s})$ to the initial channel length $(L_{if.is})$ for the respective processes:

$$\epsilon_f = \frac{\Delta L_f}{L_{if}}, \epsilon_s = \frac{\Delta L_s}{L_{is}}, \tag{1}$$

where $\epsilon_f$ and $\epsilon_s$ are dimensionless parameters representing the strain ratios for particle focusing and separation, respectively. $\Delta L_f$, $\Delta L_s$, $L_{if}$, and $L_{is}$ denote the stretching lengths and initial length of the straight channel for focusing and separation, respectively. Table 1 summarizes the dimensional variations for different stretching lengths.

## 2.2 Lateral displacement of particles

The difference in lateral displacement ratio $(\theta_1 - \theta_2)$ for binary particles is characterized by diameters $d_{p1}$ and $d_{p2}$ as described in Eq. 2 (Fallahi et al. 2020). This equation allows for analyzing the differences in lateral displacement between binary particles.

$$(\theta_1 - \theta_2) = \frac{\Delta d_L}{W} \alpha \frac{LQ^{1/2}}{W^{5/2}} (d_{p1}^2 - d_{p2}^2) \tag{2}$$

where $d_L$ represents the lateral displacement of particles, $W$ corresponds to the width of the rectangular cross section, $Q$ represents the flow rate, and $L$ denotes the straight channel length. The described relationship shows that increasing channel length under stretching increases the lateral distance between small and large particles before the large particles reach the center of the channel (where the particles achieve full focusing at ($\theta$=1/2)). This observation suggests that once the larger particles are stabilized at the center of the microchannel, any further stretching of the microchannel decreases the lateral distance between the two particle groups. Therefore, the condition ( $\theta_1$, $\theta_2$)≤1/2 was applied to Eq. 2.

## 2.3 Forces acting on particles

The forces acting on suspended particles in the fluid determine their specific equilibrium position. The dominant inertial lift forces that contribute to particle migration in a rectangular cross-section straight channel are $F_S$ (shear-induced lift force) and $F_W$ (wall-induced lift force) (Zhou et al. 2013a, 2013b). Apart from the dominant inertial lift forces, other lift forces, such as $F_R$ (rotation-induced lift force), $F_D$ (drag force), and the Saffman force, affect the particles in the fluid and change their equilibrium position. Upon entering the channel, suspended particles in the fluid experience the aforementioned forces, causing them to migrate along the streamlines. These hydrodynamic forces are determined by the flow patterns, which are directly influenced by the channel geometries (Zhou and Papautsky 2013; Zhang et al. 2016; Martel and Toner 2014). In addition to the geometric shape of the channel, factors such as particle size, density, fluid velocity, viscosity, and flow rate also affect the behavior of inertial focusing of particles, especially on the location and number of equilibrium positions (Gou et al. 2018). Among the mentioned forces, certain forces significantly impact the performance of the microchannel, while others can be considered negligible and disregarded. Table 2 presents the equations for the forces acting on particles in a straight microchannel. Further details of the forces are provided in the Supplementary Material.

## 2.4 Governing equations for fluid flow analysis

In fluid mechanics, flow patterns are classified based on Reynolds numbers. In microfluidic systems, this dimensionless parameter indicates the type of flow within the channels, which is typically laminar. The fluid density, flow velocity, channel hydraulic diameter, and fluid dynamic viscosity influence the Reynolds number. Because microchannels have small dimensions and operate at low flow rates, the Reynolds number is usually very low. A Reynolds number lower than about 2000 is typically associated with laminar flow conditions (Zhang et al. 2016; Brody and Yager 1996). In this regime, turbulence is negligible, allowing precise control of particle motion along predictable streamlines. As either flow rate or channel size increases, the Reynolds number increases and the flow can approach the transitional

**Table 1** Variations in microchannel cross-sectional area for each stretching length. The values of $L_{if}$ and $L_{is}$ of the straight channel are considered to be 5 and 10 mm, respectively

| Case | $\Delta L_f$ (mm) | $\Delta L_s$ (mm) | $\epsilon_f$ (-) | $\epsilon_s$ (-) | Width (μm) | Depth (μm) |
|---|---|---|---|---|---|---|
| 1 | 0 | 0 | 0 | 0 | 100 | 50 |
| 2 | 2 | 2 | 0.2 | 0.4 | 96 | 48 |
| 3 | 4 | 4 | 0.4 | 0.8 | 91 | 47 |
| 4 | 6 | 6 | 0.6 | 1.2 | 87 | 45 |
| 5 | - | 8 | - | 1.6 | 82 | 43 |

**Table 2** Forces acting on particles in a straight microchannel

| Force Name | Force Equation | Parameter Definition |
|---|---|---|
| Wall-induced lift force | $F_W = \frac{C_w \rho_f U_{max}^2 {d_p}^6}{{D_h}^4}$ | $C_w$ is the wall lift coefficient, $\rho_f$ denotes the fluid density, $U_{max}$ is the maximum fluid velocity, and $d_p$ is the particle diameter. The hydraulic diameter of the channel, $D_h$, is given by $D_h = 2W * H/(W + H)$, where $W$ and $H$ denote the width and depth of the microchannel, respectively |
| Shear-induced lift force | $F_S = \frac{C_s \rho_f U_{max}^2 {d_p}^3}{D_h}$ | $C_s$ is the lift coefficient |
| Drag force | $F_D = 6\pi\,\mu\, d_p U_{pf}$ | $\mu$ represents the viscosity of fluid, and $U_{pf}$ shows the normal particle velocity relative to fluid velocity |
| Inertial lift force | $F_L = \frac{f_l \rho_f {U_{max}}^2 {d_p}^4}{{D_h}^2}$ | $f_l$ is the dimensionless lift coefficient |
| Rotation-induced lift force | $F_R = \pi\, {d_p}^3 \rho_f \Omega \times U_{pf}$ | $\Omega$ represents the angular velocity of the particle |
| Saffman force | $F_s = \frac{k}{4}(u_f - u_p){d_p}^2\left(\gamma \frac{\rho_f}{\mu}\right)^{\frac{1}{2}}$ | $k$ is a numerical constant ( $k = 81.2$), $(u_f - u_p)$ represents the relative velocity between the particle and fluid flow, and $\gamma$ denotes the shear rate |

Note: References: (Zhou and Papautsky 2013; Zhang et al. 2016; Martel and Toner 2014); some symbols modified for clarity; definitions provided in the table

or turbulent range (Krishnan et al. 2017). In the simulation conducted for this research, the Reynolds number was investigated throughout the microchannel domain. A value of 1.2 was obtained, confirming that the flow remains well within the laminar regime. Therefore, laminar flow conditions with Re = 1.2 were assumed, consistent with typical microfluidic behavior. The flow dynamics in the microchannel are governed by the Navier-Stokes and continuity equations (Eqs. 3 and 4).

$$\nabla . \vec{u} = 0 \tag{3}$$

$$\rho_f \left( \frac{\partial \vec{u}}{\partial t} + \vec{u} . \nabla \vec{u} \right) = -\nabla p + \mu_f \nabla^2 \vec{u} + \vec{F} \tag{4}$$

where, $\vec{u}$ represents the vector of fluid velocity, $p$ denotes pressure, $\mu_f$ indicates fluid dynamic viscosity, and $\vec{F}$ represents the field of external forces. The fluid flow field was first calculated to trace the path of particles or cells in the microchannel. The trajectory path of particles inside the channel is determined by Newton's second law:

$$\frac{d(m_p \vec{v}_p)}{dt} = \vec{F_t} \tag{5}$$

where $m_p$ signifies the mass of particles, and $\vec{v}_p$ represents the velocity of the particles. Additionally, $\vec{F_t}$ denotes the vector that encompasses the total forces exerted on the particles. Upon solving Eq. 5, the resultant forces allow for the calculation of both the magnitude and direction of the particle. Subsequently, the vector representing the particle's position can be obtained as:

$$\frac{d(\vec{r})}{dt} = \vec{v} \tag{6}$$

## 2.5 Solution strategy

Simulations were conducted using COMSOL Multiphysics (v5.6). The computational domain was discretized with unstructured meshes, and mesh independence was ensured through convergence testing. The fluid velocity field was solved using the laminar flow physics module with a stationary solver, followed by a time-dependent solver for particle tracking. Initial and boundary conditions included a no-slip condition at channel walls, atmospheric pressure at outlets, and specified flow rates. For particle focusing, 15 µm particles were introduced with a sample flow rate of 10 $\mu$L/min and a sheath flow rate of 50 $\mu$L/min. For particle separation, binary particles (10-µm and 15-µm in diameter) were introduced, with flow rates adjusted to 10 $\mu$L/min for the sample flow and 215 $\mu$L/min for the sheath flow. Particle trajectories were modeled based on Newton's second law, incorporating dominant forces such as wall-induced lift, shear-induced lift, drag, and rotation-induced lift. Rigid boundary conditions ensured particle-wall interactions that resulted in either mirror (specular) or random (diffuse) reflections upon collision, consistent with the mixed-reflection model employed. The density and dynamic viscosity of the simulated fluid were set at 1039 kg/m$^3$ and 0.0011 Pa · s, respectively. Particles were initially distributed randomly at the central inlet and migrated to equilibrium positions at different outlets under the influence of applied forces.

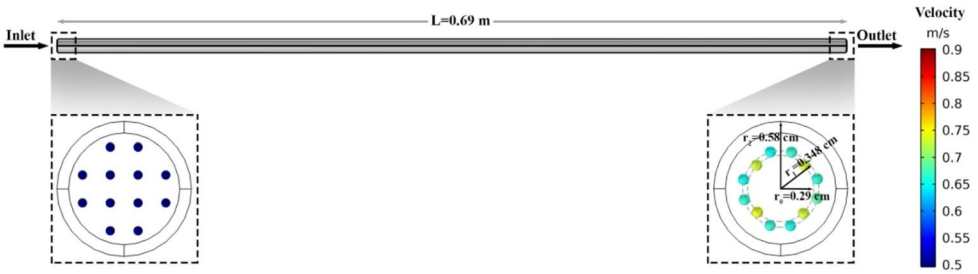


**Fig. 2** Validation of numerical approach with the experimental results of Segre and Silberberg (1961, 1962)

## 3 Results and discussion

### 3.1 Mesh study

To balance computational efficiency and accuracy in practical simulations, a mesh independence study was conducted to determine the optimal mesh. Reducing the number of mesh elements may lead to a loss of critical details, reducing solution accuracy, while increasing them extends computational time. Since complete particle focusing was achieved at a strain ratio ($\epsilon_f$) of 0.6, with a width of 87 µm and a height of 45 µm, this geometry was selected for mesh analysis. To assess mesh dependence, it is essential to ensure that the mesh size is small enough to accurately capture all changes occurring during the numerical solution. To verify the accuracy of the grid applied to the geometry, simulations were performed with several neighboring grids that closely resemble the applied grid. As longitudinal stretching of the microchannel alters the cross-sectional area and maximum velocity, it consequently affects the equilibrium position of the particles. Hence, it is crucial to verify the maximum velocity, to ensure that the chosen mesh does not produce an unusual value for the maximum velocity. Further details, including average values of velocity and shear stress (Table S1) and assessment of mesh independence with T-test statistical method (Table S2) are provided in the Supplementary Material for a more comprehensive comparison. Finally, the fine mesh (264,975 elements) was selected for the simulation due to its satisfactory accuracy. Key parameters show less than 1% variation compared to the Normal mesh, with overall error ranges within ±2% for average quantities, indicating stable and reliable results.

### 3.2 Validation

To validate the proposed numerical approach and ensure the applied settings' correctness, the geometry simulation

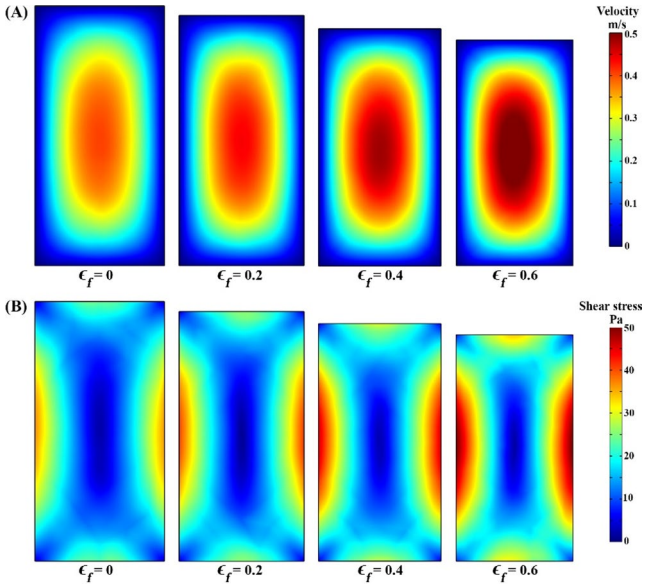


**Fig. 3** Distribution of **(A)** velocity and **(B)** shear stress at varying $\epsilon_f$ of 0, 0.2, 0.4, and 0.6, with a constant flow rate of 10 $\mu L/min$ for the sample flow and 50 $\mu L/min$ for the sheath flow. The $L_{if}$ is 10 mm

presented in the experimental study of Segre and Silberberg (1962) has been done. They observed that the particles dispersed in the tube were not focused in the centerline of the tube but were located on a narrow ring at a distance of about 0.5 to 0.6 relative to the channel radius ($0.5r_2$–$0.6r_2$). By implementing the geometry and applying the desired configuration, the settings related to the experimental study of Segre and Silberberg were fully applied in the numerical model. Figure 2 shows that the simulation results confirm the existing experimental results.

### 3.3 Laminar flow

The analysis of changes in flow patterns within the microchannel, as well as the distribution of velocity and shear

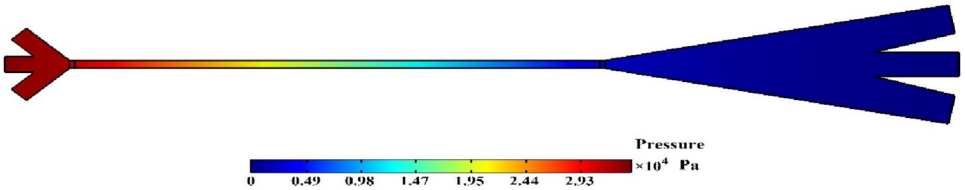


**Fig. 4** Pressure distribution in a straight microchannel. The flow rates for the sample and sheath flow are 10 and 50 µL/min respectively

stress at different $\epsilon_f$ values, is presented in Fig. 3. Figure 3A shows the velocity profile characteristics as two-dimensional cut planes at the outlet of the channel. The analysis includes cases of $\epsilon_f$ equal to 0, 0.2, 0.4, and 0.6. Generally, in a straight microchannel with a rectangular cross-section, the velocity profile exhibits a parabolic profile. Larger particles located near the centerline of the channel move faster in the direction of the flow, whereas particles near the walls exhibit slower velocities. As the stretching length increases, the cross-sectional area of the microchannel decreases, resulting in higher fluid velocity. Additionally, the fluid velocity near the walls approaches zero, indicating adherence to the no-slip condition. Figure 3B illustrates the shear stress distribution as two-dimensional cut planes at the outlet of the straight channel cross-section. The shear stress distribution reaches its minimum value at the center of the microchannel and gradually increases towards the walls, ultimately attaining its maximum value at the walls. As longitudinal stretching increases, both the velocity and shear stress fields are altered due to changes in the cross-sectional area. The decrease in the cross-sectional area of the microchannel after stretching results in an increase in fluid velocity and a corresponding decrease in shear stress at the channel center, which subsequently changes the equilibrium position of the particles and causes them to follow distinct flow paths towards specific outlets. Figure 5 indicates a gradual decrease in pressure from the inlet to the outlet, consistent with the Bernoulli principle and the pressure gradient driving the flow. Eventually, the pressure reaches atmospheric levels at the outlet. These observations highlight the accuracy of fluid flow simulations conducted within the channel.

## 3.4 Particle tracing

### 3.4.1 Particle focusing

Figure 5 illustrates the inertial focusing and corresponding equilibrium positions of 15-µm particles at different $\epsilon_f$ values (0, 0.2, 0.4, and 0.6) at the outlet of the straight microchannel with an initial length ( $L_{if}$) of 10 mm. FRR, which represents the ratio between the sample flow rate and the sheath flow rate, was maintained at a constant value of 10:50 $\mu$L/min. In Fig. 5A, where no stretch is applied to the length of the microchannel, the straight microchannel is assumed to have a length of 10 mm. In this case, the majority

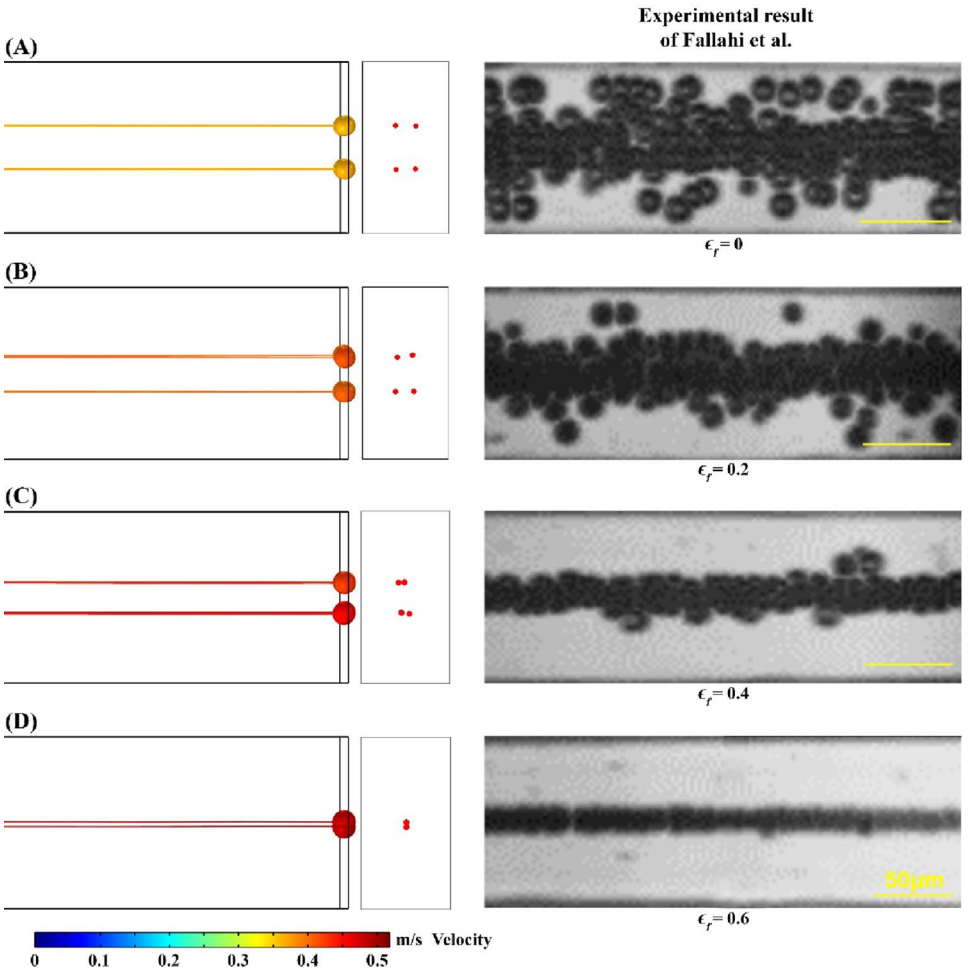


**Fig. 5** Comparison of simulation (left) and experimental (right) results (Fallahi et al. 2020) for particle inertial focusing, showing the corresponding equilibrium positions of 15-µm particles at different particle focusing strain ratios ($\epsilon_f$). The values of $\epsilon_f$ are **(A)** 0, **(B)** 0.2, **(C)** 0.4, and **(D)** 0.6. The flow rates for the sample and sheath flow are 10 and 50 $\mu$L/min, respectively. The initial length of the straight channel for focusing is $L_{if} = 10\,mm$. Adapted with permission from (Fallahi et al. 2020). Copyright 2020 American Chemical Society

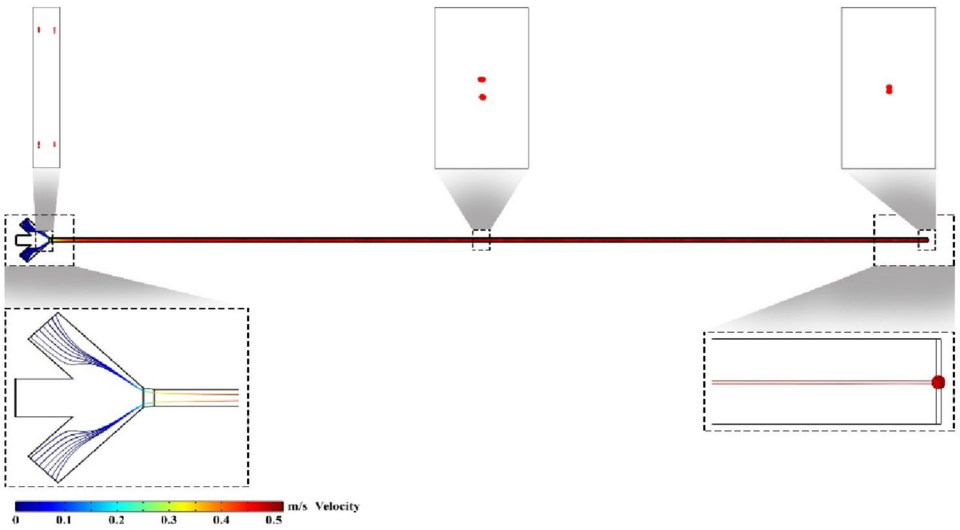


**Fig. 6** Migration behavior and focusing of 15-µm particles at $\epsilon_f = 0.6$ with a constant flow rate of 10 $\mu L/min$ for the sample flow and 50 $\mu L/min$ for the sheath flow. The $L_{if}$ is 10 mm

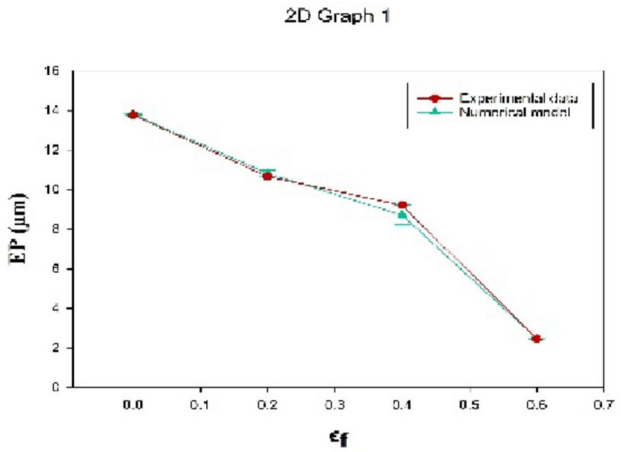


**Fig. 7** Comparison of particle equilibrium position in simulation results with experimental results (Fallahi et al. 2020) for 15-µm particles at different $\epsilon_f$ values (0, 0.2, 0.4, and 0.6). Error bars indicate the absolute deviation between simulation and experimental values, providing a measure of agreement

of particles show a scattered distribution within the channel. However, as the stretching length of the device increases, more particles migrate toward the center of the microchannel (Fig. 5B and C). Eventually, at $\epsilon_f = 0.6$, as shown in Fig. 5D, the particles are completely focused, achieving almost 100% focusing efficiency. These results indicate that stretching of the channel length significantly affects the fluid flow pattern, enhancing the lateral migration of particles toward the center of the channel, thereby improving final particle focusing. The qualitative validation of these results demonstrates strong alignment with experimental findings, indicating a high level of agreement between the simulations and practical outcomes.

On the other hand, Fig. 6 illustrates the lateral migration and progressive focusing of the particles at $\epsilon_f = 0.6$ at different points of the channel, including the inlet, middle, and outlet. The visualization is provided in both 3D and 2D cutting planes. The streamlines and the position of particles at the microchannel inlet depict variations in flow rates and show that the sheath flow is higher than the sample flow. As the channel stretches along its length, the particles gradually migrate toward the center. Tracking the particles at the middle of the microchannel demonstrates that they move closer to the center, confirming the positive effect of stretching. Finally, the particle positions at the outlet show complete focusing.

Quantitative validation was also performed to assess the agreement between the experimental and simulation results. Figure 7 compares both experimental and simulation results of the equilibrium positions of 15-µm particles at different $\epsilon_f$ values (0, 0.2, 0.4, and 0.6). The vertical axis represents the particle's equilibrium position at the outlet, while the horizontal axis indicates the different $\epsilon_f$ values. Error bars indicate the absolute deviation between the simulation and experimental values at each point, providing a quantitative measure of agreement. The results show a high degree of similarity between simulation and experimental data. The mean absolute error (MAE) of the particle equilibrium positions was 0.18% (relative MAE), corresponding to an accuracy of 99.82%. This small relative deviation indicates excellent agreement between the simulation and experimental results (Further details on the MAE calculation are provided in the Supplementary Material). The graph clearly demonstrates that an increase in the stretching length of the microchannel leads to the particles' equilibrium position moving closer to the centerline. The slight discrepancy between the experimental and simulation results in the stretching ratio range of $\epsilon_f = 0.2 - 0.4$ can be attributed to several factors. Experimental uncertainties, including

equipment calibration, variations in experimental handling, material variability, and environmental effects (García et al. 2022; Ahrens et al. 2013; Lin et al. 2025; Acosta-Cuevas et al. 2023; Akbari et al. 2023), may introduce small fluctuations that affect particle trajectories before full inertial focusing is achieved. In contrast, the simulation is based on controlled and idealized conditions, such as prescribed flow rates, simplified boundary conditions, and an idealized microchannel geometry (Lauricella et al. 2025; Wörner 2012; Avcı 2025). Although physically justified assumptions are employed in the model, these necessary simplifications may lead to minor deviations. Such discrepancies are commonly reported in microfluidic studies and fall within the expected range for simulation validation.

#### 3.4.2 Particle separation

Figure 8 presents an evaluation of the microfluidic device's performance in effectively manipulating and separating particles at different $\epsilon_s$ values, comparing these results with experimental data. Simulations were performed using a straight microchannel with an initial length ( $L_{is}$) of 5 mm at different $\epsilon_s$ values of 0, 0.4, 0.8, 1.2, and 1.6, and a mixture of binary particles with dimensions of 10- and 15-µm. The ratio of the sample to sheath flow rate was set at 10:215 $\mu l/min$ and both types of particles were randomly introduced from side inlets and meticulously tracked as they traversed the microchannel to investigate the tunability of the stretchable inertial device for particle separation. In Fig. 8A, the position of the particles in the expanding region of the microchannel outlet is depicted without the application of stretching. Due to the significant sheath flow, both small and large particles are forced towards the sidewalls. Consistent with experimental findings, the larger particles (15-µm) slightly deflect towards the center of the microchannel, while the smaller particles (10-µm) move more towards the sidewalls. However, in this case, neither particle type was successfully separated, as both entered the side outlets.

In a straight channel, particles located in the center of the channel to move faster, while those near the lateral walls move more slowly. Thus, a longer channel is more effective for particle separation, as it provides larger particles enough time to approach the center of the microchannel. This is supported by the results shown in Fig. 8B, which indicate that at $\epsilon_s = 1.2$, more 15-µm particles enter the middle outlet of the channel. These particles appear positioned along two lines within the middle outlet, showing closer proximity to the centerline of the channel. Further stretching ($\epsilon_s = 1.6$) (Fig. 8C) allows the binary particles to establish their respective equilibrium positions within the microchannel. 15-µm particles enter the middle outlet and are located along a line close to the center line of the channel. In contrast, the 10-µm particles were directed into the side outlets.

The elongated channel significantly affects the migration behavior of both particle groups by providing additional time for larger particles to approach the center. The increased differential migration achieved by the adjustable channel creates better separation. Therefore, increasing the stretch length improved the effective separation of 10- and 15-µm particles, and showed an increase in separation efficiency and purity equal to 100%. The results obtained from the particle tracing simulation under different stretching lengths demonstrate a strong correlation with Eq. 2. This relationship shows that increasing the length of the microchannel results in an increased lateral distance between the 15-µm and 10-µm particles before the larger particles reach the center of the microchannel. Once the 15-µm particles reach a stable position at the center of the microchannel, further stretching decreases the lateral distance between the binary particles. The strong consistency observed between the simulated data, experimental data, and the theoretical model confirms the precision and reliability of the proposed method. The elongated channel facilitates better separation and ensures higher purity and accuracy in the detection of particles of different sizes. By fine-tuning the channel dimensions, the separation efficiency can be precisely controlled, and highly selective sorting can be achieved, which is important for applications such as clinical diagnostics and environmental monitoring.

One of the key challenges in optimizing system performance is addressing complex real-world conditions, where changes in fluid properties or the presence of heterogeneous samples can significantly affect separation efficiency. Future research should focus on developing more precise models to accurately simulate these scenarios. Improvements in device performance include expanding channel stretchability and investigating wider dimensional variations, allowing the platform to control a wider range of particle sizes and sample properties, and increasing its adaptability for complex biological samples. Furthermore, integrating real-time monitoring systems and designing multifunctional platforms will pave the way for hybrid systems that combine multiple functions within a single device. These advancements will extend the system's applications to rare cell isolation, drug development, and point-of-care diagnostics. Finally, refining the system to manage more complex flow dynamics and incorporating it into lab-on-a-chip platforms will enhance performance and scalability, positioning this technology as an innovative and efficient solution across various fields.

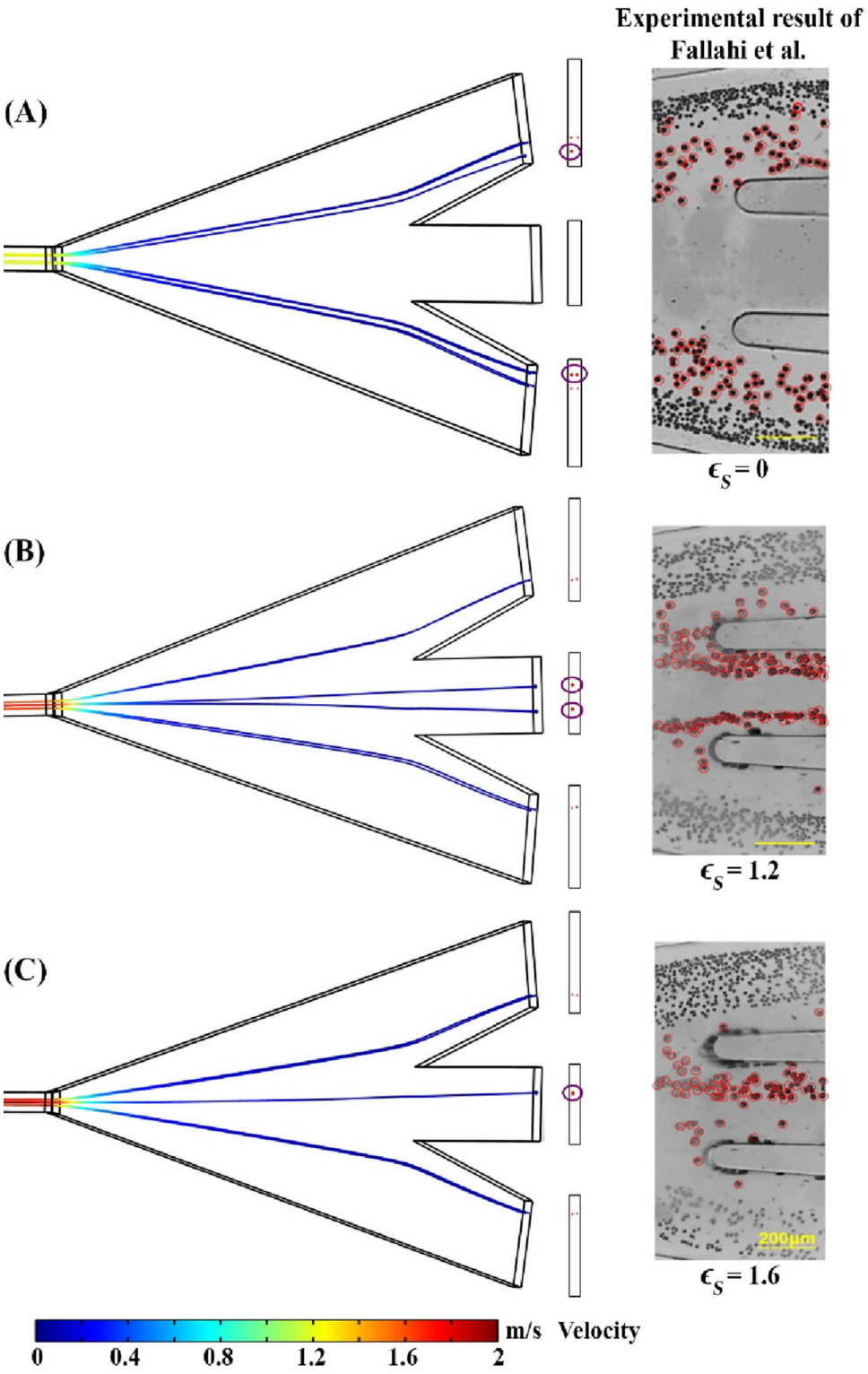


**Fig. 8** Comparison of simulation (left) with experimental (right) results (Fallahi et al. 2020) for the separation of 10-µm (black) and 15-µm (red) particles at different separation strain ratios $\epsilon_s$. The values of $\epsilon_s$ are **(A)** 0, **(B)** 1.2, and **(C)** 1.6. The 15-µm particles are marked by purple circles. The flow rates for the sample and sheath flow are 10 and 215 $\mu\, L/min$, respectively. The initial length of the straight channel for separation is $L_{is} = 5\, mm$. Adapted with permission from (Fallahi et al. 2020). Copyright 2020 American Chemical Society

## 4 Conclusion

This study presented a mathematical framework and reported 3D simulations of a stretchable inertial microfluidic device to achieve tunable particle focusing and separation. Numerical simulations revealed that channel stretching significantly improved particle focusing and separation efficiency by altering cross-sectional dimensions and fluid flow patterns. At $\epsilon_f = 0.6$, particles achieved nearly 100% focusing efficiency. Similarly, the findings

demonstrated that elongating the channel ensures higher separation efficiency for binary particle mixtures, achieving a separation efficiency and purity of 100%. As stretching increases, the 15- and 10-µm particles migrate toward distinct equilibrium positions and their respective outlets. At $\epsilon_s = 1.2$ and $1.6$, the 15-µm particles gradually shift closer to the channel center and ultimately align along a trajectory near the centerline, while the 10-µm particles are directed towards the side outlets. The qualitative and quantitative comparison of simulation results with experimental data exhibited an excellent agreement, with 99.82% accuracy, emphasizing the validity and reliability of the proposed model. The high agreement confirms the reliability of the proposed method in replicating experimental conditions and predicting system performance. The stretchable inertial microfluidic device is capable of dynamically adjusting channel dimensions on-site without the need for repeated designing, testing, optimizing, or fabricating, for enhanced particle focusing and separation. This adaptability enables comprehensive analysis of performance parameters and accurate prediction of system behavior, thereby facilitating system evaluation and optimization. The numerical simulations underscore the ability to reduce reliance on trial-and-error approaches while significantly minimizing the time and financial costs associated with device development and optimization. Additionally, the proposed setup provides a valuable framework for optimizing microchannel dimensions and operational parameters in simulations related to the manipulation of bioparticles and cells. Future studies should focus on varying key parameters such as particle size, channel stretching length, and flow rates to assess the generality and performance of the device. They should also explore more complex flow conditions and incorporate real-time monitoring systems to enable closed-loop feedback for practical applications.

### 4.1 Supplementary Information

The supplementary material provides additional supporting information for this study. It includes a detailed description of the mesh study, which validates the numerical accuracy and grid independence of the simulations. Furthermore, additional analysis regarding the forces acting on particles in a straight microchannel is presented to complement the results discussed in the main text.

**Supplementary Information** The online version contains supplementary material available at https://doi.org/10.1007/s10404-025-02869-6.

**Author contributions** S.T (Shaghayegh Tavasoli): Conceptualization, Investigation, Methodology, Formal analysis, Visualization, Software, Validation, Writing-original draft; M.S (M. Soltani): Supervision, Project administration, Writing-review & editing; M.K.S: Writing-review & editing; N.K: Supervision, Project administration, Writing-review & editing; N.-T.N: Supervision, Project administration, Writing-review & editing.

**Funding** No funding was received for conducting this study.

**Data availability** All data used for this study are available from the corresponding author upon reasonable request.

## Declarations

**Competing interests** The authors declare no competing interests.

## References

Acosta-Cuevas JM, García-Ramírez MA, Hinojosa-Ventura G, Martínez-Gómez ÁJ, Pérez-Luna VH, González-Reynoso O (2023) Surface roughness analysis of microchannels featuring microfluidic devices fabricated by three different materials and methods. Coatings 13:1676

Ahrens M, Klein S, Nestler B, Damiani C (2013) Design and uncertainty assessment of a setup for calibration of microfluidic devices down to 5 nL min−1. Meas Sci Technol 25:015301

Akbari Z, Raoufi MA, Mirjalali S, Aghajanloo B (2023) A review on inertial microfluidic fabrication methods. Biomicrofluidics. https://doi.org/10.1063/5.0163970

Altmann J, Ripperger S (1997) Particle deposition and layer formation at the crossflow microfiltration. J Membr Sci 124:119–128

Avcı M (2025) Device-oriented CFD comparison of rectangular and circular microchannels with single and double asymmetric stenoses under identical operating conditions. Bioengineering 12:1313

Ayuso JM, Virumbrales-Muñoz M, Lang JM, Beebe DJ (2022) A role for microfluidic systems in precision medicine. Nat Commun 13:3086

Baek JY, Park JY, Ju JI, Lee TS, Lee SH (2005) A pneumatically controllable flexible and polymeric microfluidic valve fabricated via in situ development. J Micromech Microeng 15:1015

Bogseth A, Zhou J, Papautsky I (2020) Evaluation of performance and tunability of a co-flow inertial microfluidic device. Micromachines 11:287

Brody JP, Yager P (1996) Low Reynolds number micro-fluidic devices, Proc. of Solid-State Sensor and Actuator Workshop, pp. 105–108

Carvalho V, Rodrigues RO, Lima RA, Teixeira S (2021) Computational simulations in advanced microfluidic devices: a review. Micromachines 12:1149

Çetin B, Li D (2011) Dielectrophoresis in microfluidics technology. Electrophoresis 32:2410–2427

Cha H, Fallahi H, Dai Y, Yuan D, An H, Nguyen N-T, Zhang J (2022) Multiphysics microfluidics for cell manipulation and separation: a review. Lab Chip 22:423–444

Chrimes AF, Khoshmanesh K, Stoddart PR, Mitchell A, Kalantar-Zadeh K (2013) Microfluidics and Raman microscopy: current applications and future challenges. Chem Soc Rev 42:5880–5906

Chung AJ, Gossett DR, Di Carlo D (2013) Three dimensional, sheathless, and high-throughput microparticle inertial focusing through geometry-induced secondary flows. Small 9:685–690

Contreras-Naranjo JC, Wu H-J, Ugaz VM (2017) Microfluidics for exosome isolation and analysis: enabling liquid biopsy for personalized medicine. Lab Chip 17:3558–3577

Del Giudice F, Madadi H, Villone MM, D'Avino G, Cusano AM, Vecchione R, Ventre M, Maffettone PL, Netti PA (2015) Magnetophoresis 'meets' viscoelasticity: deterministic separation of

magnetic particles in a modular microfluidic device. Lab Chip 15:1912–1922
Di Carlo D (2009) Inertial microfluidics. Lab Chip 9:3038–3046
Erickson D (2005) Towards numerical prototyping of labs-on-chip: modeling for integrated microfluidic devices. Microfluid Nanofluid 1:301–318
Fallahi H, Zhang J, Phan H-P, Nguyen N-T (2019) Flexible microfluidics: fundamentals, recent developments, and applications. Micromachines 10:830
Fallahi H, Zhang J, Nicholls J, Phan H-P, Nguyen N-T (2020) Stretchable inertial microfluidic device for tunable particle separation. Anal Chem 92:12473–12480
Fallahi H, Yadav S, Phan H-P, Ta H, Zhang J, Nguyen N-T (2021) Size-tuneable isolation of cancer cells using stretchable inertial microfluidics. Lab Chip 21:2008–2018
Forbes TP, Forry SP (2012) Microfluidic magnetophoretic separations of immunomagnetically labeled rare mammalian cells. Lab Chip 12:1471–1479
García BF, Mousaviraad M, Saraji S (2022) Verification and validation for microfluidic CFD simulations of newtonian and non-Newtonian flows. Appl Math Model 107:557–573
Gharib G, Bütün İ, Muganlı Z, Kozalak G, Namlı İ, Sarraf SS, Ahmadi VE, Toyran E, Van Wijnen AJ, Koşar A (2022) Biomedical applications of microfluidic devices: a review. Biosensors 12:1023
Gou Y, Jia Y, Wang P, Sun C (2018) Progress of inertial microfluidics in principle and application. Sensors 18:1762
Grier DG (2003) A revolution in optical manipulation. Nature 424:810–816
Hettiarachchi S, Cha H, Ouyang L, Mudugamuwa A, An H, Kijanka G, Kashaninejad N, Nguyen N-T, Zhang J (2023) Recent microfluidic advances in submicron to nanoparticle manipulation and separation. Lab Chip 23:982–1010
Huang LR, Cox EC, Austin RH, Sturm JC (2004) Continuous particle separation through deterministic lateral displacement. Science 304:987–990
Jeon H, Kim Y, Lim G (2016) Continuous particle separation using pressure-driven flow-induced miniaturizing free-flow electrophoresis (PDF-induced μ-FFE). Sci Rep 6:19911
Kiani Shahvandi M, Soltani M, Moradi Kashkooli F, Saboury B, Rahmim A (2022) Spatiotemporal multi-scale modeling of radiopharmaceutical distributions in vascularized solid tumors. Sci Rep 12:14582
Kimura H, Sakai Y, Fujii T (2018) Organ/body-on-a-chip based on microfluidic technology for drug discovery. Drug Metab Pharmacokinet 33:43–48
Krishnan K, Bertram O, Seibel O (2017) Review of hybrid laminar flow control systems. Prog Aerosp Sci 93:24–52
Lauricella G, Naderi MM, Owen B, Mostafazadeh N, Zhou J, Peng Z, Papautsky I (2025) Computational methods for inertial microfluidics: recent advances and future perspectives. Microsyst Nanoeng 11:202
Li W, Zhang L, Ge X, Xu B, Zhang W, Qu L, Choi C-H, Xu J, Zhang A, Lee H (2018) Microfluidic fabrication of microparticles for biomedical applications. Chem Soc Rev 47:5646–5683
Lin J, Cui L, Shi X, Wu S (2025) Emerging trends in microfluidic biomaterials: from functional design to applications. J Funct Biomater 16:166
Martel JM, Toner M (2014) Inertial focusing in microfluidics. Annu Rev Biomed Eng 16:371–396
Mashhadian A, Shamloo A (2019) Inertial microfluidics: a method for fast prediction of focusing pattern of particles in the cross section of the channel. Anal Chim Acta 1083:137–149
Mukherjee J, Chaturvedi D, Mishra S, Jain R, Dandekar P (2024) Microfluidic technology for cell biology–related applications: a review. J Biol Phys 50:1–27
Nouri M, Parvizian P, Nikookalam A, Seifi S, Shamloo A (2024) A numerical study of elasto-inertial particle-focusing in straight and serpentine microchannels. Results Eng 23:102640
Park J, Kim YW, Jeon H-J (2024) Machine learning-driven innovations in microfluidics. Biosensors 14:613
Pinho D, Muñoz-Sánchez BN, Anes CF, Vega E, Lima R (2019) Flexible PDMS microparticles to mimic RBCs in blood particulate analogue fluids. Mech Res Commun 100:103399
Raoufi MA, Mashhadian A, Niazmand H, Asadnia M, Razmjou A, Warkiani ME (2019) Experimental and numerical study of elasto-inertial focusing in straight channels. Biomicrofluidics. https://doi.org/10.1063/1.5093345
Sajeesh P, Sen AK (2014) Particle separation and sorting in microfluidic devices: a review. Microfluid Nanofluid 17:1–52
Scheler O, Postek W, Garstecki P (2019) Recent developments of microfluidics as a tool for biotechnology and microbiology. Curr Opin Biotechnol 55:60–67
Segre G, Silberberg A (1961) Radial particle displacements in poiseuille flow of suspensions. Nature 189:209–210
Segre G, Silberberg A (1962) Behaviour of macroscopic rigid spheres in poiseuille flow part 2. Experimental results and interpretation. J Fluid Mech 14:136–157
Shahvandi MK, Souri M, Tavasoli S, Kashkooli FM, Kar S, Soltani M (2023) A comparative study between conventional chemotherapy and photothermal activated nano-sized targeted drug delivery to solid tumor. Comput Biol Med 166:107574
Sheidaei Z, Akbarzadeh P, Kashaninejad N (2020) Advances in numerical approaches for microfluidic cell analysis platforms. J Science: Adv Mater Devices 5:295–307
Souri M, Kiani Shahvandi M, Chiani M, Moradi Kashkooli F, Farhangi A, Mehrabi MR, Rahmim A, Savage VM, Soltani M (2023) Stimuli-sensitive nano-drug delivery with programmable size changes to enhance accumulation of therapeutic agents in tumors. Drug Deliv 30:2186312
Tajik P, Saidi MS, Kashaninejad N, Nguyen N-T (2019) Simple, cost-effective, and continuous 3D dielectrophoretic microchip for concentration and separation of bioparticles. Ind Eng Chem Res 59:3772–3783
Tu C, Zhou J, Liang Y, Huang B, Fang Y, Liang X, Ye X (2017) A flexible cell concentrator using inertial focusing. Biomed Microdevices 19:1–12
Vu HH, Nguyen N-T, Nguyen N-K, Luu CH, Hettiarachchi S, Kashaninejad N (2023) Tunable wettability with stretchable microstructured surfaces. Adv Eng Mater 25:2300821
Wang X, Papautsky I (2015) Size-based microfluidic multimodal microparticle sorter. Lab Chip 15:1350–1359
Wang Z, Zhe J (2011) Recent advances in particle and droplet manipulation for lab-on-a-chip devices based on surface acoustic waves. Lab Chip 11:1280–1285
Wörner M (2012) Numerical modeling of multiphase flows in microfluidics and micro process engineering: a review of methods and applications. Microfluid Nanofluid 12:841–886
Yamada M, Seki M (2005) Hydrodynamic filtration for on-chip particle concentration and classification utilizing microfluidics. Lab Chip 5:1233–1239
Yamada M, Nakashima M, Seki M (2004) Pinched flow fractionation: continuous size separation of particles utilizing a laminar flow profile in a pinched microchannel. Anal Chem 76:5465–5471
Yang Y, Chen Y, Tang H, Zong N, Jiang X (2020) Microfluidics for biomedical analysis. Small Methods 4:1900451
Zhang J, Li W, Li M, Alici G, Nguyen N-T (2014) Particle inertial focusing and its mechanism in a serpentine microchannel. Microfluid Nanofluid 17:305–316
Zhang J, Yan S, Yuan D, Alici G, Nguyen N-T, Warkiani ME, Li W (2016) Fundamentals and applications of inertial microfluidics: a review. Lab Chip 16:10–34

Zhang SP, Lata J, Chen C, Mai J, Guo F, Tian Z, Ren L, Mao Z, Huang P-H, Li P (2018a) Digital acoustofluidics enables contactless and programmable liquid handling. Nat Commun 9:2928

Zhang J, Yuan D, Zhao Q, Yan S, Tang S-Y, Tan SH, Guo J, Xia H, Nguyen N-T, Li W (2018b) Tunable particle separation in a hybrid dielectrophoresis (DEP)-inertial microfluidic device. Sens Actuators B Chem 267:14–25

Zhang S, Wang Y, Onck P, den Toonder J (2020) A concise review of microfluidic particle manipulation methods. Microfluid Nanofluidics 24:24

Zhang T, Inglis DW, Ngo L, Wang Y, Hosokawa Y, Yalikun Y, Li M (2023) Inertial separation of particles assisted by symmetrical sheath flows in a straight microchannel. Anal Chem 95:11132–11140

Zhou J, Papautsky I (2013) Fundamentals of inertial focusing in microchannels. Lab Chip 13:1121–1132

Zhou T, Liu Z, Wu Y, Deng Y, Liu Y, Liu G (2013a) Hydrodynamic particle focusing design using fluid-particle interaction. Biomicrofluidics. 7. https://doi.org/10.1063/1.4821170

Zhou J, Giridhar PV, Kasper S, Papautsky I (2013b) Modulation of aspect ratio for complete separation in an inertial microfluidic channel. Lab Chip 13:1919–1929

Zhou T, Deng Y, Zhao H, Zhang X, Shi L, Joo S. Woo (2018) The mechanism of size-based particle separation by dielectrophoresis in the viscoelastic flows. J Fluids Eng 140:091302

Zhou J, Kulasinghe A, Bogseth A, O'Byrne K, Punyadeera C, Papautsky I (2019) Isolation of circulating tumor cells in non-small-cell-lung-cancer patients using a multi-flow microfluidic channel. Microsyst Nanoeng 5:8

Zhou T, Ji X, Shi L, Zhang X, Song Y, Joo SW (2020a) AC dielectrophoretic deformable particle-particle interactions and their relative motions. Electrophoresis 41:952–958

Zhou Y, Ma Z, Ai Y (2020b) Dynamically tunable elasto-inertial particle focusing and sorting in microfluidics. Lab on a Chip 20:568–581

Zhou T, He X, Zhao J, Shi L, Wen L (2023) Electrokinetic transport of nanoparticles in functional group modified nanopores. Chin Chem Lett 34:107667